# Chandra Observations of the Lensing Cluster EMSS 1358+6245: Implications for Self-Interacting Dark Matter

J.S. Arabadjis<sup>1</sup>, M.W. Bautz<sup>1</sup>, and G.P. Garmire<sup>2</sup>

#### ABSTRACT

We present Chandra observations of EMSS 1358+6245, a relaxed cooling flow cluster of galaxies at z=0.328. We employ a new deprojection technique to construct temperature, gas, and dark matter profiles. We confirm the presence of cool gas in the cluster core, and our deprojected temperature profile for the hot component is isothermal over 30 kpc < r < 0.8 Mpc. Fitting the mass profile to an NFW model yields  $r_s=153^{+161}_{-83}$  kpc and  $c=8.4^{+3.4}_{-2.3}$ . We find good agreement between our dark matter profile and weak gravitational lensing measurements. We place an upper limit of 42 kpc (90% confidence limit) on the size of any constant density core. We compare this result to recent simulations and place a conservative upper limit on the dark matter particle scattering cross section of  $0.1~{\rm cm^2~g^{-1}}$ . This limit implies that the cross-section must be velocity dependent if the relatively shallow core mass profiles of dwarf galaxies are a direct result of dark matter self-interaction.

Subject headings: X-rays: galaxies: clusters — cosmology: dark matter

#### 1. Introduction

Galaxy clusters are powerful laboratories wherein to test the structure formation theories and simulations of modern cosmology. For example, while enjoying many successes in explaining a large number of observational results (Navarro, Frenk & White 1996, 1997; Moore et al. 1999), the cold dark matter (CDM) paradigm appears to be inconsistent with details of the structure of cluster dark matter halos (Spergel & Steinhardt 2000) and galactic rotation and density profiles (Spergel & Steinhardt 2000; Moore et al. 1999). The question of

<sup>&</sup>lt;sup>1</sup>Center for Space Research, Massachusetts Institute of Technology, Cambridge, MA 02139; jsa@space.mit.edu, mwb@space.mit.edu

 $<sup>^2\</sup>mathrm{Department}$  of Astronomy & Astrophysics, 525 Davey Laboratory, The Pennsylvania State University, University Park, PA 16802

whether a CDM universe can produce the observed mass profiles of galaxy clusters without serious modification is currently unresolved, although the emerging consensus is that CDM alone probably fails to produce cluster cores like those observed (e.g. Spergel & Steinhardt (2000); Davé et al. (2001); Yoshida et al. (2000); see Taylor & Navarro (2001), however).

The launch of the Chandra X-ray Observatory (Weisskopf et al. 2000) has made it possible to study the mass distribution in the central regions of galaxy clusters where the discrepancies between CDM models and observations are the most glaring (Moore et al. 1999; Firmani et al. 2000). The  $\sim 0.$ "5 spatial resolution of the Chandra/ACIS-S instrument, which corresponds to about 3 kpc at z=0.3, is now comparable to that of ground-based optical measurements, (although in practice low-N photon statistics limits the actual resolution achieved). For nearby clusters, for sufficiently long exposures, one can measure the mass profile of a cluster in the inner few kpc (David et al. 2001), scales which are generally inaccessible to gravitational lensing studies.

The advantage possessed by gravitational lensing studies, however, is that the measurement is independent of the dynamical state of the gravitating matter. To derive a total gravitating mass profile from the baryonic X-ray emission map one assumes hydrostatic equilibrium (Sarazin 1988; Allen & Fabian 1994), which in practice means that one assumes that the cluster is supported via isotropic thermal pressure (i.e.  $v_{\rm rot}/\sigma \ll 1$  and  $|\mathbf{B}|^2/nkT \ll 1$ ), and that no recent merger event has caused a disruption in the pressure, temperature and density profiles. One would expect clusters with fairly circular isophotes, and which contain cooling flows (which are thought to be disrupted in merging events – see Allen & Fabian (1997), Allen (1998) and Fabian et al. (2001)), to merit the simplifying hydrostatic treatment.

EMSS 1358+6245 (a.k.a. CL 1358+6245, ZwCl 6249) is such a galaxy cluster. Discovered optically by Zwicky (Zwicky & Herzog 1968) and later in X-rays with the Einstein IPC (Luppino et al. 1991), it is a nearly circular, apparently relaxed cluster, with an Abell richness class 4 (Luppino et al. 1991; Hoekstra et al. 1998) and a central bright cooling flow (Bautz 1997; Allen 1998). Because of its moderate redshift (z=0.328), the entire cluster fits on the ACIS S3 chip, leaving enough blank field to derive a reliable background estimate. Figure 1 shows a broad band (0.3-7.0 keV) ACIS S3 image of EMSS 1358+6245, adaptively Gaussian smoothed on scales of 1 to 10 pixels ( $\sim$ 0.5 to 5"). The contour levels are listed from inner- to outermost; contours associated with point sources in the field have been omitted. The presence of the cooling flow and the regularity of the X-ray isophotes suggest that hydrostatic equilibrium is a reasonable approximation of the dynamical state of the cluster gas. Figure 2 shows a mosaic of archived HST exposures of the central region of EMMS 1358+6245 with adaptively-smoothed soft-band (0.3-2.0 keV) X-ray isophotes su-

perimposed. Note that the peak of the emission (i.e. the central green dot), at a value of  $2.95 \text{ photons}/(0.''49)^2$ , appears to be slightly offset from the position of the central dominant galaxy (CDG). We shall return to this point in §2.

The mass of EMSS 1358+6245 has been measured using both weak (Hoekstra et al. 1998) and strong (Franx et al. 1997; Allen 1998) gravitational lensing, and estimated from ASCA and ROSAT observations (Bautz 1997; Allen 1998). These measurements are roughly consistent, with a mass of about  $4 \times 10^{14}~M_{\odot}$  enclosed within the 1 Mpc. In this study, we use a Chandra ACIS-S imaging spectroscopy to derive a mass profile of EMSS 1358+6245 and compare it to lensing measurements.

We briefly outline the Chandra observation and data analysis procedure in §2. We describe our deprojection and modelling technique in §3, and compare our results to previously published measurements in §4. We then use our profile to constrain possible dark matter matter candidates in §5. Finally we summarize our findings in §6. We assume  $\Omega_m = 1$ ,  $\Omega_{\Lambda} = 0$ , and  $H_0 = 50h_{50}$  km s<sup>-1</sup> Mpc<sup>-1</sup> throughout (1" = 5.79 kpc at z = 0.328 for  $h_{50} = 1$ ).

## 2. Chandra Observations, Astrometry, and Data Analysis

EMSS 1358+62 was observed with the Chandra X-ray Observatory for approximately 55 ks on 3-4 September 2000 using the S3 chip on the ACIS detector. The level 2-processed data were aspect-corrected and filtered for periods of high background using the CIAO software package, according to the standard procedures described in the CIAO Science Threads (2001).

The center of the projected X-ray emissivity (Figure 2) is offset from the optical position of the CDG by about 2" (about 12 kpc). The offset, if real, has important consequences for the dynamical state of the cluster, so we carefully examined the the astrometry of the Chandra field. We ran the CIAO wavelet source detection routine wavdetect (CIAO Science Threads 2001) on the ACIS S2/S3 fields (i.e. those chips closest to the ACIS-S aimpoint), and cross-correlated the output with the Tycho-2 (Høg et al. 2000) and USNO-A2.0 (Monet et al. 1998) catalogues. Five USNO sources and zero Tycho sources were within 3" of a wavlet-detected Chandra source. Figure 3 shows the location of the five USNO sources in relation to the Chandra ACIS S2/S3 field, the HST mosaic, and the CDG. Although the Tycho-2 catalogue is nominally more accurate than the USNO-A2.0 catalogue, with internal astrometric standard errors in general less than 90 mas (Høg et al. 2000), above  $\delta = -20$  the USNO positions are usually within 20 mas of the Tycho-2 positions (Assafin et al. 2001), making USNO-A2.0 as effective an astrometric standard. Of these five sources, two appear

somewhat extended, either because they are galaxies or because they are sufficiently far from the ACIS aim point. The remaining three point sources were used as astrometric anchors to calculate the difference between the Chandra and USNO coordinates. These offsets are shown as filled circles in Figure 4. The mean offset is represented by the small open circle, and its error by the ellipse. About half of the CDG/X-ray peak offset is due to the Chandra field astrometry. Figure 5 shows the center of the cluster including this astrometric correction. The top panel shows broad-band (0.3-7.0 keV) X-ray contours superimposed on the 0-10 pixel adaptively smoothed,  $2 \times 2\text{-binned}$  broad-band Chandra image. The same contours are also shown on the unsmoothed  $2 \times 2\text{-binned}$  Chandra image (middle) and on the central field of the HST mosaic (bottom). The offset between the CDG and the X-ray peak that remains after the astrometric correction is 0.''99, while the error in the correction is 0.''97. Therefore, the CDG and the X-ray emission peak are cospatial at about the  $1\text{-}\sigma$  level.

After locating the center of the projected emissivity we divided the cluster into 10 concentric annuli such that each contained a minimum of 2000 counts (1600-2000 after background subtraction), the center annulus being a disk. Owing to decreased signal-to-noise in the outer bins, annuli 9 and 10 were constructed to contain roughly 4000 (2700) and 10,000 (3300) photons, respectively. We found that the extra counts in the last two annuli were required for numerical stability during the iterative fitting procedure, and they also helped to reduce the "noise" in the derived temperature profile. The annuli ranged (outer radius) from 11.5 to 285.8 pixels, which translates to 5.66 to 140.56 arcsec. At z = 0.328, this corresponds to  $\sim 30$  to 800 kpc, for  $H_0 = 50$  km s<sup>-1</sup> Mpc<sup>-1</sup> and  $q_0 = 0.5$  (see Table 1).

All obvious point sources were removed, and a spectrum was extracted from each annulus. RMF and ARF response matrices were constructed according to the CIAO Science Threads (2001), as was a background spectrum from an annulus exterior to the outermost bin. The spectra were recorded in PI format, and grouped such that there were a minimum of 20 counts per channel.

#### 3. Cluster Deprojection and Mass Determination

We assume that the cluster is a spherical, self-gravitating pressure-supported plasma whose X-ray emission is optically thin. We assume hydrostatic equilibrium throughout (except for small blobs of cold gas in the innermost regions which, although not hydrostatic, are assumed to be in a steady state). The hydrostatic equation can be written (Sarazin 1988)

$$M(r) = -\frac{kT}{G\mu m_p/r} \left( \frac{d\log T}{d\log r} + \frac{d\log \rho}{d\log r} \right) , \qquad (1)$$

where T and  $\rho$  are the local (baryonic) gas temperature and density, r is the spherical radius, M(r) is the total mass enclosed within r (i.e. baryons plus dark matter), and  $m_p$  and  $\mu$  are the proton mass and mean particle weight, respectively.

To check our assumption of spherical symmetry we examined the surface brightness map for deviations from circular symmetry. Specifically, we performed a simple analysis to estimate the ellipticity  $\epsilon$  (and position angle  $\theta$ ) of the cluster elongation. We calculate the luminosity of a pair of wedges A, centered on the X-ray peak of the cluster, and compare it to a second pair B perpendicular to the first (see Figure 6). The wedges have semiwidth  $\delta$ , radius  $R_A$  (or  $R_B$ ), and phase  $\theta$  (or  $\theta + \pi/2$ ). The luminosity of the two wedge pairs is then

$$L_A(R_A, \theta) = \int_0^{R_A} r dr \left[ \int_{\theta - \delta}^{\theta + \delta} \Sigma(\theta, r) d\theta + \int_{\theta + \pi - \delta}^{\theta + \pi + \delta} \Sigma(\theta, r) d\theta \right]$$
 (2)

and

$$L_B(R_B, \theta) = \int_0^{R_B} r dr \left[ \int_{\theta + \pi/2 - \delta}^{\theta + \pi/2 + \delta} \Sigma(\theta, r) d\theta + \int_{\theta + 3\pi/2 - \delta}^{\theta + 3\pi/2 + \delta} \Sigma(\theta, r) d\theta \right]$$
(3)

Maximizing  $L_A(\theta)$  for  $R_A/R_B=1$  yields the position angle, and then scaling  $R_B/R_A$  until  $L_A/L_B=1$  gives an estimate of the axial ratio, which is simply  $1+\epsilon$ . The noise in the surface brightness map that tends to inflate  $L_A/L_B$  for some  $\theta$  is ameliorated somewhat by the smoothing introduced by the finite window size  $\delta$ . Figure 7 shows the axial ratio and position angle as a function of  $R_A$ . The flattening is consistent with an ellipticity of 0.34 over an order of magnitude in  $R_A$ , for  $\delta=\pi/36$ . Because much of this flattening is due to substructure in the soft emission due to the cool component (which shows an axial ratio of 2.5 for  $R_A=200$ ), we feel confident that the assumption of spherical symmetry, especially in the hot, pressure-dominating component, is not unreasonable. We shall, however, return to the implications of  $\epsilon=0.3$  in §5.

Se also fit a 2-D  $\beta$  model to the cluster emission map using the Sherpa data analysis package (CIAO Science Threads 2001). The profile is described by

$$f(x,y) = \frac{f_0}{\left(1 + \frac{r^2}{r_0^2}\right)^{3\beta - \frac{1}{2}}} \tag{4}$$

where

$$r = \sqrt{u^2 + v^2/(1 - \epsilon)^2} , \qquad (5)$$

u and v are the rotated coordinates:

$$\begin{pmatrix} u \\ v \end{pmatrix} = \begin{pmatrix} \cos\theta + \sin\theta \\ -\sin\theta + \cos\theta \end{pmatrix} \begin{pmatrix} x \\ y \end{pmatrix} , \tag{6}$$

and  $\epsilon$  and  $\theta$  are the isophotal ellipticity and position angle, respectively. (We have assigned (x,y)=0 to the X-ray emission peak.) Here  $r_0$  is the core radius and  $f_0$  is the central surface brightness. We fit for the core radius, the amplitude, and the isophotal ellipticity and orientation. We use the maximum likelihood method of Cash (1979), as implemented in Sherpa (CIAO Science Threads 2001), rather than a  $\chi^2$  minimization, because the vast majority of the image pixels contain fewer than  $\sim 20$  photons.

We find an ellipticity of  $0.174\pm0.008$  for the cluster (the position angle has an oblate/prolate degeneracy), although the uncertainty is underestimated due to parameter correlations. This indicates again that spherical symmetry is a reasonable approximation. The best fit parameter values are  $r_0 = 130 \pm 30$  kpc and  $\beta = 0.69 \pm 0.02$ .

In order to derive spherical radial profiles we construct a model consisting of N concentric spherical shells whose inner and outer radii correspond to the inner and outer cylindrical radii of the projected annuli in the data set. (Hereafter annuli/shells will be labeled 1 through N, in order of increasing radius.) Quantities can be mapped between the two geometries through the upper diagonal matrix V, whose elements  $V_{ij}$  contain the volume of spherical shell j intersected by a cylindrical shell formed by the projection of annulus i. If the volume emissivity of the gas in spherical shell j is  $u_j$ , then the luminosity of annulus i,  $H_i$ , is simply

$$\mathbf{H} = \mathsf{V} \cdot \mathbf{u} \;, \tag{7}$$

where we have written the relation for all annuli simultaneously. Since H is related to the surface brightness I through  $H_j = 2\pi (r_j^2 - r_{j-1}^2)I$ , the deprojection of the surface brightness is accomplished by inverting V, which is completely specified by the binning geometry. Because V is upper diagonal, the solution set of volume emissivities is easily obtained working from the outer- to the innermost annulus. The emissivity of the outermost shell is simply  $u_N = H_N/V_{NN}$ , while the rest of the shells are calculated moving inward using

$$u_{j} = \frac{2\pi(r_{j}^{2} - r_{j-1}^{2})I_{j} - \sum_{i=j+1}^{N} V_{ji} \cdot u_{i}}{V_{jj}}$$
(8)

The volume emissivity of each spherical shell is characterized by a temperature and a normalization. The X-ray emission from each shell is modelled spectroscopically using MEKAL (Mewe, Gronenschild & van den Oord 1986; Mewe, Lemen & van den Oord 1986; Kaastra 1992; Liehdal, Osterheld & Goldstein 1995) model in the XSPEC software package (Arnaud 1996), which describes the emission from an optically thin thermal plasma.

Since a strong cooling flow signature was seen in both ASCA and ROSAT observations (Bautz 1997; Allen 1998), we first sought to verify its existence in the Chandra data. We modelled the inner two annuli separately using the cooling flow model CFLOW of Mushotzky & Szymkowiak (1988) in XSPEC, together with a MEKAL component and an intervening absorber. The cooling flow model is described by a mass deposition rate M, a hot gas temperature and a low-temperature cut-off. We assume that the flow cools from the ambient cluster gas, so we pinned the hot gas temperature to the MEKAL temperature during the fitting procedure. We also assume that the emissivity is proportional to the inverse cooling time at the local temperature. An acceptable fit ( $\chi^2/\text{d.o.f.} = 62.37/69$ ) was obtained for a mass deposition rate of  $40.1^{+6.9}_{-18.9}~M_\odot~{\rm y}^{-1}$  (90% confidence interval) and a low-T cut-off  $\sim 1$  keV. This result differs significantly from that of Allen (1998), who finds  $\dot{M} = 690^{+350}_{-290}$  $M_{\odot}/y$ . The discrepancy is due to the extra (internal) absorption component which that study assigns to the cooling flow emission. While we find no particularly compelling reason to incorporate an additional absorber in this type of model (Arabadjis & Bregman 2000), we do not argue this point in the present study, since we merely wish to establish the presence of a cool emission component in the Chandra data.

The bulk of the emission in the flow originates from the coolest gas, and so in the interest of simplicity we modelled the cooling flow component in the complete cluster analysis as a second MEKAL component, rather than with the CFLOW model. To determine the appropriate spatial extent of the cool gas we tried adding a second emission component (at lower temperature) to several of the inner spherical shells. (We shall refer to these two temperatures as  $T_h$  and  $T_c$ , for the hot cluster gas and the cooling flow gas, respectively.) We ran models with two components in (A) shell 1, (B) shells 1 and 2, (C) shells 1 through 3, and (D) 1 through 4. Model B had a lower reduced chi-squared value than did model A, and the temperature and normalizations of cool components in models C and D were essentially unconstrained. We therefore adopted B as our working model, and note that this suggests that the cool gas extends out to about 70 kpc. It should also be noted that,

unlike other deprojection methods, this method makes no assumptions about the shape of the temperature and density profiles other than spherical symmetry and the finite width of radial bins.

The number of concentric shells that can used to construct this model is limited by two quantities, the memory allocation of the XSPEC program and the number of photons above the background in the spectrum. An active XSPEC model is limited to 1000 parameters, with only 100 allowed to vary at any time. Each MEKAL component contains 6 parameters, but we allow only kT and the normalization to vary. In addition, we include an intervening column of Galactic material which absorbs all emission components equally. For N concentric annuli in the data, there are  $N + N_2$  emission components, where  $N_2$  is the number of two-component shells. Including the absorbing column yields a model with  $6(N + N_2) + 1$  parameters. This model is applied to N data sets, with the normalizations across them scaled by the appropriate geometric factors (i.e. ratios of V terms). Thus the complete XSPEC model contains  $N[6(N + N_2) + 1]$  components, with  $2(N + N_2) + 1$  of them variable. In our case we had  $N_2 = 2$  two-component shells, thus limiting N to 11.

In practice, however, we found that we had to limit N to 10 because the finite number of photons in our 55 ks spectrum caused instability during the numerical iteration if the temperature of any given shell was sufficiently unconstrained. It turns out that  $\gtrsim 1800$  source photons per annulus are required to bring the "noise" in the fitted temperature profile to a level where numerical stability is achieved throughout the iterative process, which in our case resulted in 10 annuli (using  $N_2 = 2$ ). Thus our model contains a total of 730 parameters, with 25 of these floating, well under the XSPEC limit.

The best-fit model has a chi-squared of 942.4 for 891 degrees of freedom (there are 916 spectral bins in the data). The temperature and density profiles are shown in Figure 8. The model shown at left allows the temperature of each shell to vary. Note that the temperature profile is consistent with isothermality, with an error-weighted average temperature of  $7.16 \pm 0.10$  keV, while the right side pins all the shells at 7 keV. In each case the second emission component is shown as the pair of points near R = 0.1 and 0.2 arcsec. The inferred density profiles are nearly indistinguishable.

The temperature and density profiles can be used to derive an entropy profile of the cluster. The discovery of an "entropy floor" in galaxy clusters (Ponman, Cannon & Navarro 1999) and its subsequent measurement in many clusters (Lloyd-Davies, Ponman, & Cannon 2000) have led groups to attempt to explain it in terms of an additional source of heat (SNe and/or AGN activity) which acts either to preheat the gas that collapses to form the cluster, or which heats the cluster throughout its formation (Balogh, Babul & Patton 1999; Loewenstein 2000; Wu, Fabian & Nulsen 2000). The specific entropy of the cluster baryons

can be calculated using

$$S = T n_e^{-2/3} (9)$$

where  $n_e$  is the electron number density of the gas. In Figure 9 we plot the entropy profile of the cluster. The cold gas entropy is shown for the inner two shells as well. The entropy of the hot cluster gas toward the center is consistent with the entropy floor of 70-140 keV cm<sup>2</sup> reported by Lloyd-Davies, Ponman, & Cannon (2000) in their sample of 20 clusters.

The temperature and density profiles can also be used according to equation 1 to measure the total gravitating mass in the cluster. Figure 10 shows the mass profiles corresponding to the temperature/density profiles of Figure 8, with the logarithmic derivatives calculated as simple differences. The data points in the left panel represent M(r), the mass contained within spherical radius r, calculated using the density and unrestricted temperature profile shown in the left panels of Figure 8. The solid blue curve represents the best-fit "universal density profile" of Navarro, Frenk & White (1996, 1997), hereafter the NFW profile, a two-parameter family of models whose functional form is

$$\frac{\rho(r)}{\rho_0} = \left(\frac{r}{r_s}\right)^{-1} \left(1 + \frac{r}{r_s}\right)^{-2} \tag{10}$$

where  $r_s$  is a scale length,  $\rho_0 = \delta_c \, \rho_{crit}(z)$ , and  $\delta_c$  is a characteristic (dimensionless) density dependent upon the formation epoch of the dark matter halo.  $\rho_{crit}(z)$  is the critical density at the observed redshift; for a matter-dominated,  $\Omega_0 = 1$ ,  $\Lambda = 0$  universe this is

$$\rho_{crit} = \frac{3H_0^2}{8\pi G} (1+z)^3 \tag{11}$$

The total mass scales as  $h^{-1}$ , so our baryon fraction is weakly dependent upon h. Of course, radial distances such as  $r_s$  scale as  $h^{-1}$ .

We report our best-fit values as  $r_s$  and c, the concentration parameter, defined by

$$\delta_c = \frac{\rho_0}{\rho_{crit}} = \frac{200}{3} \frac{c^3}{\ln(1+c) - c/(1+c)}$$
 (12)

In practice, because the form of our mass profile is M(r) and not  $\rho(r)$ , we use the integrated mass of the NFW profile as our fitting template, rather than the density:

$$M(r) = M_0 \left[ \ln(1 + r/r_s) + (1 + r/r_s)^{-1} - 1 \right]$$
(13)

where  $M_0 = 4\pi \rho_0 r_s^3$ . Using M(r) rather than  $\rho(r)$  spares us one numerical differentiation, which would augment the profile noise considerably. We find  $r_s = 153^{+161}_{-83}$  kpc and  $c = 8.4^{+3.4}_{-2.3}$ .

Kelson et al. (2000) have measured the central velocity dispersion of the galaxy located at the cluster center using the Keck I 10m telescope. Using the low-resolution imaging spectrograph with a square 1.05" aperture, they infer a central velocity dispersion of 311 $\pm$ 11 km s<sup>-1</sup>. From HST photometry they obtain an effective radius of r = 3.9" (23 kpc). Assuming a singular isothermal density profile with an istropic velocity dispersion, the enclosed mass is given by:

$$M_{iso}(r) = \frac{2\sigma^2 r}{G} \tag{14}$$

The dashed black line at left (Figure 10) represents an isothermal sphere at  $\sigma = 311$  km s<sup>-1</sup>, with the Kelson et al. (2000) measurement shown as a filled circle plotted at the effective radius. Although the point barely falls within the 1- $\sigma$  envelope, it should be remembered that this point is a model extrapolation from the aperture radius. If one uses the aperture radius rather that the effective radius, the point lies very near the NFW best-fit line. We shall return to this point in §5.

The solid blue curve at the right half of Figure 10 shows the best-fit  $(\chi^2/d.o.f. = 2.1/6)$  spherical NFW profile projected along the line of sight, i.e.  $M(r) \to M(R)$  (in order to compare with the surface density maps derived from weak lensing measurements; see §4). Integrating equation 10 along the line of sight yields (Bartelmann 1996)

$$M(R) = 4\pi \rho_0 r_s^3 \cdot \begin{cases} \ln(x/2) + \frac{1}{\sqrt{1-x^2}} \operatorname{arctanh}\sqrt{1-x^2} & x < 1\\ \ln(x/2) + 1 & x = 1\\ \ln(x/2) + \frac{1}{\sqrt{x^2-1}} \operatorname{arctan}\sqrt{x^2-1} & x > 1 \end{cases}$$
(15)

where  $x = R/r_s$ .

Because of the "noise" in the solution, one point in the mass profile is unphysical. This is caused by a 1- $\sigma$  jog in the temperature profile at the seventh annulus. The (positive) logarithmic temperature gradient between annuli 6 and 7 swamps the density gradient (see

equation 1) causing M(r) < 0; this is represented in Figure 10 by an open dashed box at an arbitrary ordinate.

In order to ascertain whether this jog represents an unseen feature in the data or a fundamental flaw in the method, rather than an ordinary statistical fluctuation, we varied the initial conditions in the fitting procedure to see if the iterative process would converge to a solution lacking such a temperature anomaly. After many attempts we found that we could only move the jog to a different annulus. As a more rigorous check on the method, we analyzed a cluster simulated with MARX that contained 10<sup>5</sup> photons and no background (J. Houck & M. Wise, private communication). We derived a mass profile for this cluster using 12 annuli, and found two unphysical points due to jogs in the otherwise smooth temperature profile. We therefore conclude that the single unphysical point in our mass profile for EMSS 1358+62 is not due to undetected peculiarities in the data, but is more likely a nonexceptional statistical fluctuation. We note here that in their deprojection analysis of Hydra A, David et al. (2001), who used a smooth parametric temperature profile, were still forced to effectively smooth across radial bins in order to reduce the "noise" in the mass profile, even though they had roughly 5 times the number of photons at their disposal.

Nonetheless, we ran the model again, pinning  $T_h$  at 7 keV, to see what effect this would have on the mass profile. The resulting temperature and density profiles are shown on the right side of Figure 8. The effect on the mass profile, and its NFW fit, is small; the scale length increases from  $\sim 153$  to 197 kpc, and concentration decreases from 8.4 to 7.0. The significance of these values will be discussed in §5 below.

The gas mass and total gravitating mass profiles are shown in Figure 11, for the model wherein  $T_h$  is allowed to vary. The  $T_h = 7$  keV model is very similar. The gas mass fraction rises from  $\sim 0.025$  at 50 kpc to 0.18 at 0.6 Mpc, scaling as  $h_{50}^{-1.5}$  (White & Fabian 1995). This is consistent with the study of White & Fabian (1995), who find baryon fractions of 0.10–0.22 for a sample of 13 clusters (90% confidence). The mass of an isothermal sphere based on the Kelson et al. (2000) measurement, and its corresponding profile, is also shown, as a filled circle and a dashed line, respectively. Although these data do not allow us to distinguish between the gas, stars, and dark matter associated with the CDG, they clearly demonstrate that the total galaxy mass dominates the gas mass within the cluster center.

Our model does not allow us to determine the morphology of the cool gas within the inner two shells of cluster gas, although from our ellipticity estimation we suspect that it is fairly aspherical. However, its mass, density, and volume are completely specified, since we have assumed pressure equilibrium between the two temperature components. For the unconstrained temperature profile model, roughly 10% of the core volume is filled with cold gas, dropping to a tenth this value at the adjacent shell. Table 2 lists the relevant quantities

for both gas components in the inner two shells. We note that the broadband (0.3-7.0 keV) X-ray luminosity of the cool gas component in the inner shells is  $4.4 \times 10^{43}$  erg s<sup>-1</sup>, comparable to the luminosity of the "X-ray overluminous" ellipticals studied by Vikhlinin et al. (1999).

### 4. Comparison with Lensing Studies

In order to assess the robustness of our derived mass profiles, we compare them to the the weak lensing profile of Hoekstra et al. (1998). While gravitational lensing measurements may suffer from biases introduced by distant, uncorrelated large-scale structure, the effect on the mass determination is expected to be small for distant, rich clusters; for example, Hoekstra (2001) finds a typical  $1\sigma$  uncertainty of about 6% for measurements out to 1.5  $h_{50}^{-1}$  Mpc. In addition, Allen (1998) has shown that lensing and X-ray mass determinations are consistent provided one takes into account the presence of the lower temperature gas in the cooling flow.

Because weak lensing mass profiles measure mass within a projected radius, we integrate the best-fit NFW profile (equation 10) along the line of sight (equation 15). For both our treatments of the temperature profile of the baryons (i.e. variable vs. frozen at 7 keV), the resulting mass profile agrees well with the weak lensing profile. The strong lensing measurement (Franx et al. 1997; Allen 1998) at 120 kpc exceeds the X-ray and weak lensing measurements by a factor of  $\sim 1.6$ . We note that although the lensing results we quote and our X-ray measurement assume spherical symmetry, Hoekstra et al. (1998) find evidence for an elliptical mass distribution with an axis ratio of  $\sim 0.3$ . Our analysis shows that while the X-ray surface brightness is very nearly circular at large radii, the axis ratio in the core could be as small as 0.7. The assumption of spherical symmetry leads to an average overstimate of a factor of 1.6 in strong-lensing analyses of simulated clusters, which are generally not spherically symmetric (Bartelmann 1995).

Following Allen, Ettori & Fabian (2001) we compute an "effective velocity dispersion" of our best-fit mass profile. Using the NFW halo virial mass in the singular isothermal profile we obtain  $\sigma \equiv \sqrt{50}H(z)\,r_s c = 700^{+203}_{-84}~{\rm km~s^{-1}}$ . This is substantially lower than the observed line-of-sight velocity dispersion of Fisher et al. (1998),  $1027 \pm 50~{\rm km~s^{-1}}$ . As noted by Fisher et al., the optical velocity dispersion is probably inflated by substructure along the line of sight to the cluster. As expected, our effective velocity dispersion agrees, within measurement errors, with the value of  $\sigma = 780 \pm 50~{\rm km~s^{-1}}$  derived by Hoekstra et al. (1998) by fitting an isothermal sphere to the weak lensing data.

## 5. Constraints on Self-interacting Dark-Matter

Much has been made of the failure of CDM simulations to reproduce the observed structure of dark matter halos. A particular example of the problem is that CDM halos are steeper than observed dwarf galaxy halos. Parameterizing the core profile as  $\rho(r) = \rho_0(r/r_0)^{\alpha}$ as  $r \to 0$ , CDM simulations suggest either  $\alpha = -1$  (Navarro, Frenk & White 1996, 1997) or -1.5 (Moore et al. 1999; Fukushige & Makino 2001). H $\alpha$  observations low-surface brightness galaxies suggest a flatter profile,  $\alpha \equiv -0.5$  (Swaters, Madore & Trewhella 2001; Dalcanton & Bernstein 2000). Instead of a triaxial, central cusp, as predicted by CDM simulations, Tyson et al. (1998) find a spherical  $r_s = 35h^{-1}$  kpc core in the strong gravitational lens CL 0024+1654 using a multiply-imaged background galaxy (see Broadhurst et al. (2000) and Shapiro & Iliev (2000), however). A weak lensing study by Smail et al. (2000) also indicates soft cores CL 1455+22 and CL 0016+16. The literature survey of Firmani et al. (2000) suggests that the central density of clusters is about 0.02  $M_{\odot}$  pc<sup>-3</sup>, regardless of halo mass, whereas CDM predicts values of  $\geq 1~M_{\odot}~{\rm pc}^{-3}$  for dwarf galaxies, and larger still for more massive halos. Spergel & Steinhardt (2000), Firmani et al. (2000), Davé et al. (2001) and others use these discrepancies to argue for the existence of self-interacting dark matter (SIDM), which will tend to reduce both the core profile slope and central density of dark matter halos.

X-ray measurements of cluster dark matter profiles, however, fall somewhat more in line with the CDM simulations. Tamura et al. (2001) find a central slope of  $\sim -1.5$  for Abell 1060. Markevitch et al. (1999) find that NFW provides a good description of the mass profiles they derive for A2199 and A496 from ASCA and ROSAT observations, over the entire range for which they are able to derive a temperature profile. Allen, Ettori & Fabian (2001) observed A2390 using the ACIS S3 detector on Chandra and derive a mass profile which is consistent with the NFW profile, and find a concentration c=4, as predicted by CDM. Schmidt, Allen & Fabian (2001) also find adequate agreement between their mass profile of A1835, derived from a Chandra ACIS-S3 observation, and the NFW profile, and consistency with weak lensing measurements. They calculate a scale radius of  $640^{+210}_{-120}~{\rm kpc}$ and a concentration of  $4.0^{+0.54}_{-0.64}$ . They find a slightly better fit when they model A1835 as a non-singular isothermal sphere, deriving a core size for the cluster (distinct from the scale radius of an NFW fit) of  $r_c = 65^{+5}_{-10}$  kpc. David et al. (2001) determine a central slope of  $\alpha \sim -1.3$  for Hydra A, and find no evidence for a flat, SIDM dominated core, down to scales of  $\sim 40 \, h_{50}^{-1}$  kpc. However, their NFW fit to their mass profile results in a concentration c = 12, a factor of 3 larger than that predicted by CDM.

In general we find that the NFW model provides an adequate fit to our mass profile. Like the David et al. (2001) study, however, our fit to the mass profile of EMSS 1358+6245

results in a concentration which is somewhat higher than that predicted by NFW for rich clusters. The appendix of Navarro, Frenk & White (1997) provides a prescription for calculating cluster parameters at the collapse (i.e. formation) redshift  $z_{coll}$ , which is a function of cluster mass in this model. Using the Einstein-de Sitter simulation with a CDM spectrum normalization  $\sigma_8 = 0.63$  and h = 0.5 (the SCDM model of Navarro, Frenk & White (1997)) we calculate a collapse redshift of  $z_{coll} = 4.9$ ; it is doubtful that a cluster this massive could have formed so early. NFW predicts a concentration of about 4 for massive clusters, but the scatter in their suite of simulations could be as high as 2.

One might ask at what level SIDM can be ruled out by current observations. Recently, Yoshida et al. (2000) simulated cluster-sized halos and found that relatively small dark matter cross-sections ( $\sigma_{dm} = 0.1 \text{ cm}^2 \text{ g}^{-1}$ ) produce relatively large (40  $h^{-1}$  kpc) cluster cores. Davé et al. (2001) simulated galaxy-sized halos and required interaction cross-sections as large as 5 cm<sup>2</sup> g<sup>-1</sup> to reproduce the shallow central slopes of galaxy density profiles. As noted by Davé et al. (2001) and explored by Firmani et al. (2001), these findings can be reconciled if the dark matter interaction cross-section is velocity-dependent. For example, the two findings are roughly consistent with

$$\sigma_{dm} = \sigma_0 \left(\frac{V}{V_0}\right)^{-a} \tag{16}$$

with  $\sigma_0 = 1$  cm<sup>2</sup> g<sup>-1</sup>,  $V_0 = 100$  km s<sup>-1</sup>, and a = -1. Hennawi & Ostriker (2001), however, use supermassive black hole demographics to rule out SIDM cross sections as large as this. They present a model with a = 0 and  $\sigma_0 = 0.02$  cm<sup>2</sup> g<sup>-1</sup> that is consistent with observed supermassive black hole masses. While their model does not remedy the galactic-scale dark matter halo problem, they sketch a scenario wherein the density cusps in such halos can be softened through black hole mergers.

Our mass profile for EMSS 1358+6245 shows no evidence for a flat core on scales larger than  $40 \, h_{50}^{-1}$  kpc. In Figure 12 we show power law fits to the mass profile as a function of the outermost point used in the fit. The profile is consistent with  $M_r \propto r^{1.1}$ , or  $\alpha = -1.9$ , somewhat steeper than CDM predictions. In fact, the inner profile displays behavior which is the *opposite* of what would be required for nearing a flat core;  $\alpha$  should approach, not diverge from, 0 as  $r \to 0$ . (The restriction is even more stringent since our model uses  $H_0 = 50 \, \mathrm{km \ s^{-1} \ Mpc^{-1}}$ .) We place an upper limit on the core size by modeling the profile as a softened isothermal sphere:

$$\rho(r) = \frac{\sigma^2}{2\pi G(r^2 + r_c^2)},$$
(17)

We find a core size  $r_c = 12^{+30}_{-12} h_{50}^{-1}$  kpc (90% confidence;  $\chi^2/d.o.f. = 4.2/6$ ). The contribution of the CDG to the mass profile for r > 30 kpc is sufficiently small (Figure 10) that we can directly compare our core size limit,  $r < 42 \, h_{50}^{-1}$  kpc, with Yoshida et al. (2000). The most conservative limit we can place must include the flattening that we determined in §3. Although the cluster as a whole exhibits an ellipticity of 0.34, it could be higher toward the core (see Figure 7. The worst-case scenario would be that our innermost annulus just grazes the minor axis of a core; in that case our limit should be scaled upward by a factor of  $1 + \epsilon$ . Furthermore, in keeping with a conservative posture, if we assume that the axial ratio in the core (near r = 35 kpc; see Figure 7) is as high as 7/4, then our core limit is 74 kpc, allowing us to conservatively rule out SIDM with  $\sigma_{dm} \geq 0.1$  cm<sup>2</sup> g<sup>-1</sup>.

In order to strengthen the case for the core size upper limit, we verified that our deprojection and modelling technique can indeed detect a core if one is present. We created a set of five simulated galaxy cluster observations to which we applied our deprojection and fitting method. Each simulated cluster follows a  $\beta$  model surface brightness profile, with  $\beta = 0.69$ . The  $\beta$  model core radii  $r_0$  ranged from 6 to 96 ACIS S-3 pixels (34.7 to 556 kpc), increasing by a factor of 2 for each successive cluster. Otherwise the simulated clusters are similar to EMSS 1358+6245-z=0.328, and the photons are sampled from a distribution at T=7keV. In addition, each of the 10 annuli contains  $\sim 2000$  photons. Once we have fit for the temperature and gas density of each shell, the mass profile computed using the hydrostatic equation, which is then fit using a non-singular isothermal sphere. The resulting fits, shown in Figure 13, demonstrate that we can detect core structures in the mass profile. (The agreement between  $r_0$  and  $r_c$  might at first seem too good, particularly when one considers that  $r_0$ is a projected beta model core radius, while  $r_c$  is a spherical softened isothermal sphere core radius. However, we are pinning down the shape of the mass profile near the core radius, where the non-singular isothermal sphere is actually a good approximation to a beta model. At  $r = r_c$ , for  $\beta = 0.69$ , the agreement is better than 5%.)

In Figure 14 we plot the SIDM cross section constraints of several groups. The hatch marks delineate the region excluded by each constraint. The parameter space external to the triangular region is ruled out by Hennawi & Ostriker (2001) by requiring that SIDM (1) removes the halo cusp in dwarf galaxies, (2) does not cause core collapse in 20 km s<sup>-1</sup> halos, and (3) does not cause galactic-mass halos to evaporate in a Hubble time. Hennawi & Ostriker (2001) rule out other areas not shown here by considering the formation of supermassive black holes (SMBHs), specifically the lack of a bulge/SMBH in M33, and the presence of a bulge/SMBH in the Milky Way. They arrive at SIDM which is unable to remedy the cuspy halo problem of dwarf galaxies, and and we direct the interested reader to that study. We have indicated the results of computer simulations of Yoshida et al. (2000) and Davé et al. (2001) (see arrows). Our mass profile of EMSS 1358+6245, in conjunction

with the Yoshida et al. (2000) simulations, provide the constraint  $\sigma_{dm}(1000) < 0.1 \text{ cm}^2 \text{ g}^{-1}$ , ruling out the space indicated in blue. We observe that the core collapse and halo evaporation constraints of Hennawi & Ostriker (2001) appear to rule out the model of Davé et al. (2001) in which SIDM is responsible for dwarf galaxy halo cores. We note in passing that our observations are consistent with, though less restrictive than, the constraints derived by Hennawi & Ostriker (2001) from SMBH demographics.

While our central profile is consistent with NFW, it is intriguing that the average density within the inner 50 kpc of our mass profile is  $\sim 0.025~M_{\odot}~{\rm pc^{-3}}$ , consistent with the Firmani et al. (2000) sample. If the Kelson et al. (2000) measurement of the (assumed isotropic) velocity dispersion at 0.55" is extrapolated to  $r_e = 3.9"$  (22 kpc) as described in section §3, the resulting density is, perhaps coincidentally,  $\rho \sim 0.022 \pm 0.005~M_{\odot}~{\rm pc^{-3}}$ , suggesting that the data allow the density profile to be flat from 20 to 50 kpc. It is important to remember, however, that this extrapolation assumes that it is appropriate to characterize the CDG density profile as a singular isothermal sphere over the range  $1.05" \leq R \leq 3.91"$ . (More conservatively, if the isothermal model is assumed to hold only at the aperture radius, the profile is consistent with the absence of a core.)

However uncertain, this result is interesting because it is contrary to what would be expected from a dark halo associated with the central galaxy, and may offer a clue to the existence of SIDM which flattens cluster cores on scales of 40 kpc. The issue can be addressed with a deeper Chandra observation to enable one to probe the mass profile in X-rays down to the effective radius of the Kelson et al. (2000) measurement, or through similar observations of other relaxed clusters.

On the other hand, we note that dark halos of CDGs would steepen the central density profile and possibly complicate detection of a very small, flat SIDM core. Ironically, the relaxed nature of rich clusters, which allows us to measure their masses by assuming hydrostatic equilibrium, may turn out to obfuscate the details of the dark matter distribution. Even so, Chandra mass profiles appear to justify high-resolution N-body simulations with very low ( $\sigma < 0.1 \text{ cm}^2 \text{ g}-1$ ) dark matter interaction cross sections.

## 6. Summary

We have used a new spectral deprojection technique to derive a dark matter profile from a Chandra observation of EMSS 1358+6245. Our mass profile is consistent with optical weak lensing measurements (Hoekstra et al. 1998). It is nominally consistent with an NFW profile, although our derived concentration larger than expected from CDM simulations by a factor

of a few. Our best-fit NFW profile is characterized by  $r_s = 153^{+161}_{-83}$  kpc and  $c = 8.4^{+3.4}_{-2.3}$ . We also model the cluster as a non-singular isothermal sphere and place an upper limit on the core size  $r_c < 42 \, h_{50}^{-1}$  kpc (90% confidence). Comparing this value to the simulations of Yoshida et al. (2000), we rule out self-interacting dark matter with cross sections  $\sigma_{dm} \ge 0.1$  cm<sup>2</sup> g<sup>-1</sup>.

JSA and MWB would like to thank Paul Steinhardt and Marie Machacek for useful discussions of dark matter candidates and self-interacting dark matter, and Claude Canizares for proofreading this manuscript. JSA would like to thank Joe Hennawi and Jerry Ostriker for a pre-preprint version of their paper.

#### REFERENCES

- Allen, S.W. 1998, MNRAS, 296, 392
- Allen, S.W., Ettori, S. & Fabian, A.C. 2001, MNRAS, 324, 877
- Allen, S.W. & Fabian, A.C. 1997, MNRAS, 286, 583
- Allen, S.W. & Fabian, A.C. 1994, MNRAS, 269, 409
- Arabadjis, J.S. & Bregman, J.N. 2000, ApJ, 536, 144
- Arnaud, K.A. 1996, Astronomical Data Analysis Software and Systems V, George H. Jacoby & Jeannette Barnes, eds., ASP Conf. Ser., 101, 17
- Assafin, M., Andrei, A.H., Vieira Martins, R., da Silva Neto, D.N., Camargo J.I.B., Teixeira, R. & Benevides-Soares P. 2001, ApJ, 552, 380
- Balogh, M.L., Babul, A. & Patton, D.R., 1999, MNRAS, 307, 463
- Bartelmann, M., 1995, A&A, 299, 11
- Bartelmann, M., 1996, A&A, 313, 697
- Bautz, M.W., Honda, E.P., Ventrella, J. & Gendreau, K.C. 1997, in *Proc. Int. Symp. on X-ray Astron.*, X-Ray Imaging and Spectroscopy of Cosmic Hot Plasmas, ed. F. Makino & K. Mitsuda (Tokyo: Universal Acad. Press), 75
- Broadhurst, T., Huang, X., Frye, B., & Ellis, R. 2000, ApJ, 534, 15
- Buote, D.A. & Tsai, J.C. 1996, ApJ, 457, 565
- Cash, W. 1979, ApJ, 228, 939
- CIAO Science Threads, http://asc.harvard.edu/ciao/documents\_threads.html
- Dalcanton, J.J. & Bernstein, R.A. 2000, in XVth IAP Meeting, Dynamics of Galaxies: From the Early Universe to the Present, eds. F. Combes, G.A. Mamon & V. Charmandaris
- Davé, R., Spergel, D.N., Steinhardt, P.J. & Wandelt, B.D. 2001, ApJ, 547, 574
- David, L.P., Nulsen, P.E.J., McNamara, B.R., Forman, W., Jones, C., Ponman, T., Robertson, B., and Wise, M. 2001, ApJ, in press (astro-ph/0010224)
- Fabian, A.C., Mushotzky, R.F., Nulsen, P.E.J. & Peterson, J.R. 2001, MNRAS, 321, L20

Firmani, C., D'Onghia, E., Avila-Reese, V., Chincarini, G. & Hernández, X. 2000, MNRAS, 315, L29

Firmani, C., D'Onghia & Chincarini, G. 2001, preprint (astro-ph/0010497)

Fisher, D., Fabricant, D., Franx, M. & van Dokkum, P.G., 1998, ApJ, 498, 195

Franx, M., Illingworth, G.D., Kelson, D.D., van Dokkum, P.G. & Tran, K.-V. 1997, ApJ, 486, L75

Fukushige, T. & Makino, J., 2001, ApJ, in press (astro-ph/0008104)

Hennawi, J.F. & Ostriker, J.P., 2001, preprint (astro-ph/0108203)

Hoekstra, H., 2001, A&A, 370, 743

Hoekstra, H., Franx, M. & Kuijken, K. 1998, ApJ, 504, 636

Høg, E., Fabricius, C., Makarov, V.V., Urban, S., Corbin, T., Wycoff, G., Bastian, U., Schwekendiek, P. & Wicenec, A. 2000, A&A, 355, L27

Høg, E., Fabricius, C., Makarov, V.V., Bastian, U., Schwekendiek, P., Wicenec, A., Urban, S., Corbin, T. & Wycoff, G., 2000, A&A, 357, 367

Kaastra, J.S. 1992, An X-Ray Spectral Code for Optically Thin Plasmas, Internal SRON-Leiden Report, version 2.0.

Kelson, D.D., van Dokkum, P.G., Franx, M. & Illingworth, G.D. 1997, ApJL, 478, L13

Kelson, D.D., Illingworth, G.D. van Dokkum, P.G. & Franx, M., 2000, ApJ, 531, 159

Liedahl, D.A., Osterheld, A.L. & Goldstein, W.H. 1995, ApJL, 438, L115

Lloyd-Davies, E.J., Ponman, T.J. & Cannon, D.B., 2000, MNRAS, 315, 689

Loewenstein, M., 2000, ApJ, 532, 17

Luppino, G.A., Cooke, B.A., McHardy, I.M. & Ricker, G.R. 1991, AJ, 102, 1

Markevitch, M., Vikhlinin, A., Forman, W. R. & Sarazin, C. L. 1999, ApJ, 527, 545

Mewe, R., Gronenschild, E.H.B.M. & van den Oord, G.H.J. 1985, A&AS, 62, 197

Mewe, R., Lemen, J.R. & van den Oord, G.H.J. 1986, A&AS, 65, 511

Monet, D.G., et al. 1998, USNO-A2.0 (Washington: US Nav. Obs.)

Moore, B., Quinn, T., Governato, F., Stadel, J. & Lake, G. 1999, MNRAS, 310, 1147

Mushotzky, R.F. & Szymkowiak, A.E. 1988, in *Cooling Flows in Clusters and Galaxies*, ed. A.C. Fabian (Dordrecht: Kluwer), 53

Navarro, J.F., Frenk, C.S., and White, S.D.M. 1997, ApJ, 462, 563

Navarro, J.F., Frenk, C.S., and White, S.D.M. 1997, ApJ, 490, 493

Ponman, T.J., Cannon, T.J. & Navarro, J.F., 1999, Nature, 397, 135

Sarazin, C.L. 1988, "X-ray Emission from Clusters of Galaxies", Cambridge Astrophysics Series, Cambridge: Cambridge University Press

Schmidt, R.W., Allen, S.W. & Fabian, A.C., 2001, MNRAS, in press (astro-ph/0107311)

Shapiro, P.R. & Iliev, I.T., 2000, ApJL, 542, L1

Smail, I., Ellis, R., Ritchett, M.J. & Edge, A.C. 1995, MNRAS, 273, 277

Spergel, D.N., and Steinhardt, P.J. 2000, Phys. Rev. Lett., 84, 17

Swaters, R.A., Madore, B.F. & Trewhella, M. 2000, ApJ, 531, L107

Tamura, T., Makishima, K., Fukazawa, Y., Ikebe, Y., & Haiguang, X., 2000, ApJ, 535, 602

Taylor, J.E. & Navarro, J.F. 2001, preprint (astro-ph/0104002)

Tyson, J.A., Kochanski, G.P. & Dell'Antonio, I.P. 1998, ApJL, 498, L107

Vikhlinin, A., McNamara, B.R., Hornstrup, A., Quintana, H., Forman, W., Jones, C. & Way, M. 1999, ApJL, 520, L1

Weisskopf, M., Tananbaum, H., Van Speybroeck, L. & O'Dell, S. 2000, Proc. SPIE 4012, 2

White, D.A. & Fabian, A.C. 1995, MNRAS, 273, 72

Williams, L.L.R., Navarro, J.F. & Bartelmann, M., 1999, ApJ, 527, 535

Wu, K.K.S., Fabian, A.C. & Nulsen, P.E.J., 2000, MNRAS, 318, 889

Yoshida, N., Springel, V., White, S.D.M., & Tormen, G., 2001, ApJL, 544, L87

Zwicky, F., and Herzog, E. 1968, "Catalog of Galaxies and Clusters of Galaxies, Vol. IV, Calfornia Institute of Technology, Pasadena

This preprint was prepared with the AAS LATEX macros v5.0.

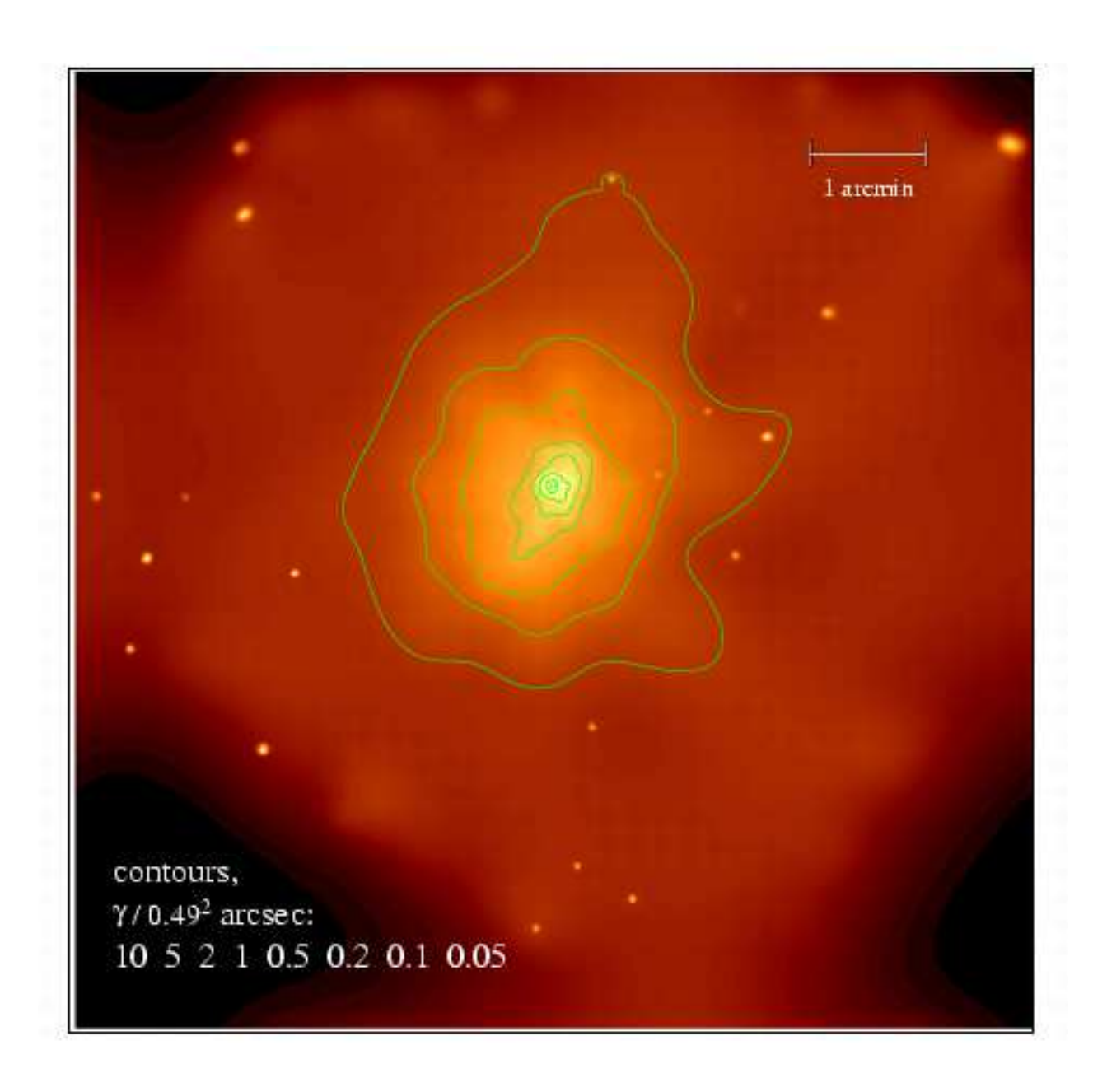


Fig. 1.— Broadband (0.3  $\leq E/{\rm keV} \leq$  7.0) image of EMSS1358+6245.

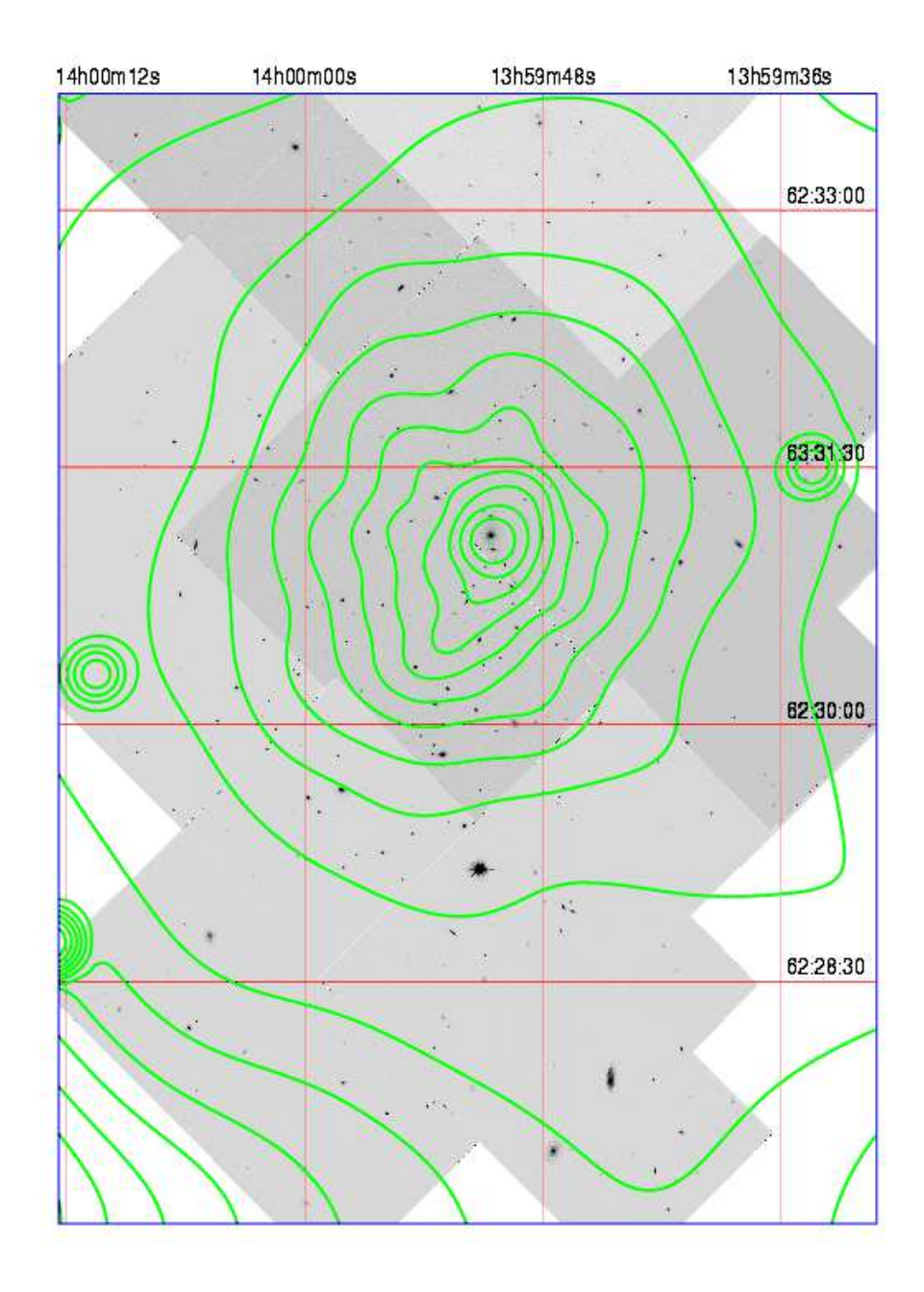


Fig. 2.— An HST image of EMSS 1358+6245 with superimposed soft X-ray (0.3  $\leq E \leq$  2.0 keV) contours. Each contour level is 3/5 of the previous value.

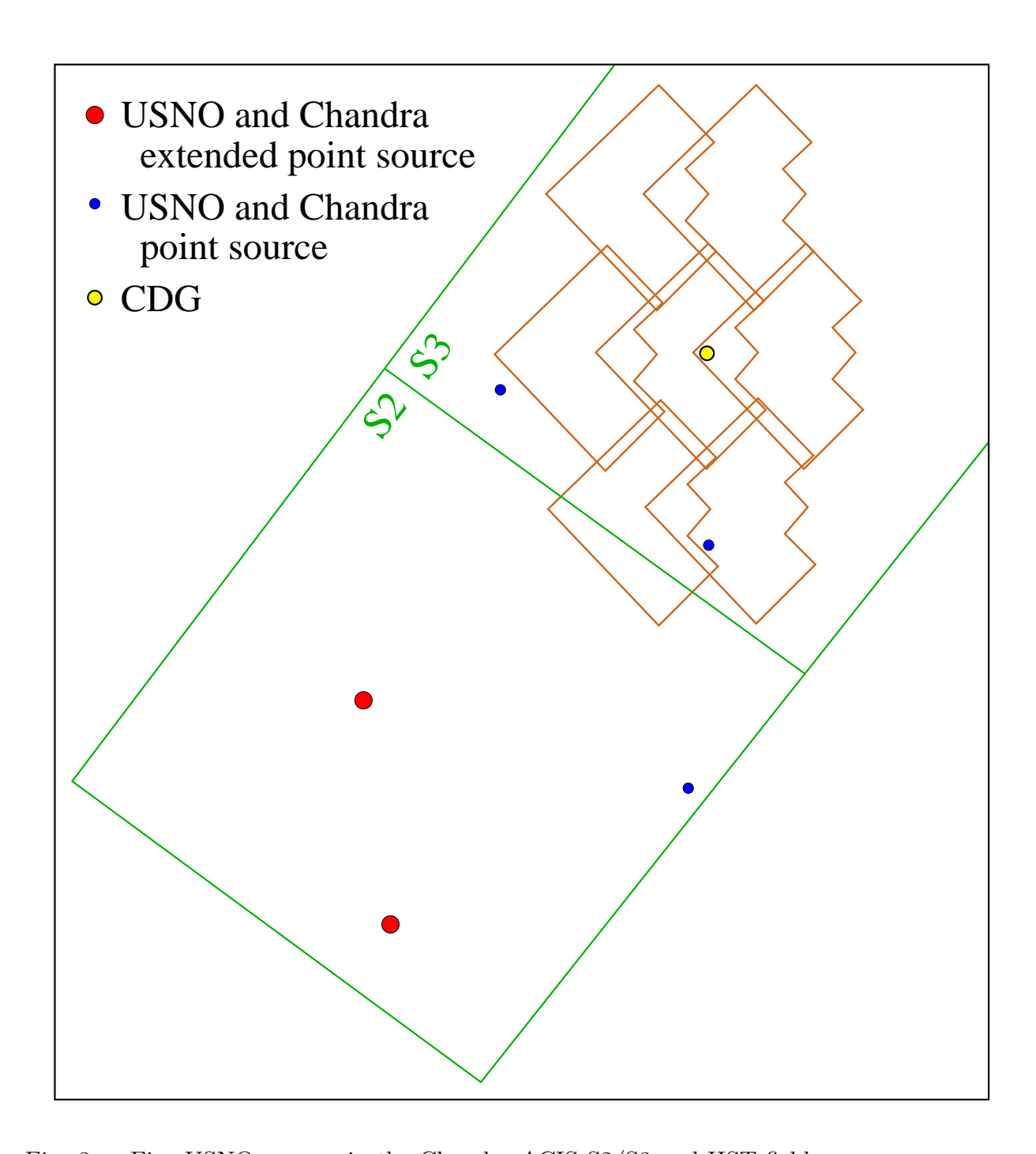


Fig. 3.— Five USNO sources in the Chandra ACIS S2/S3 and HST fields.

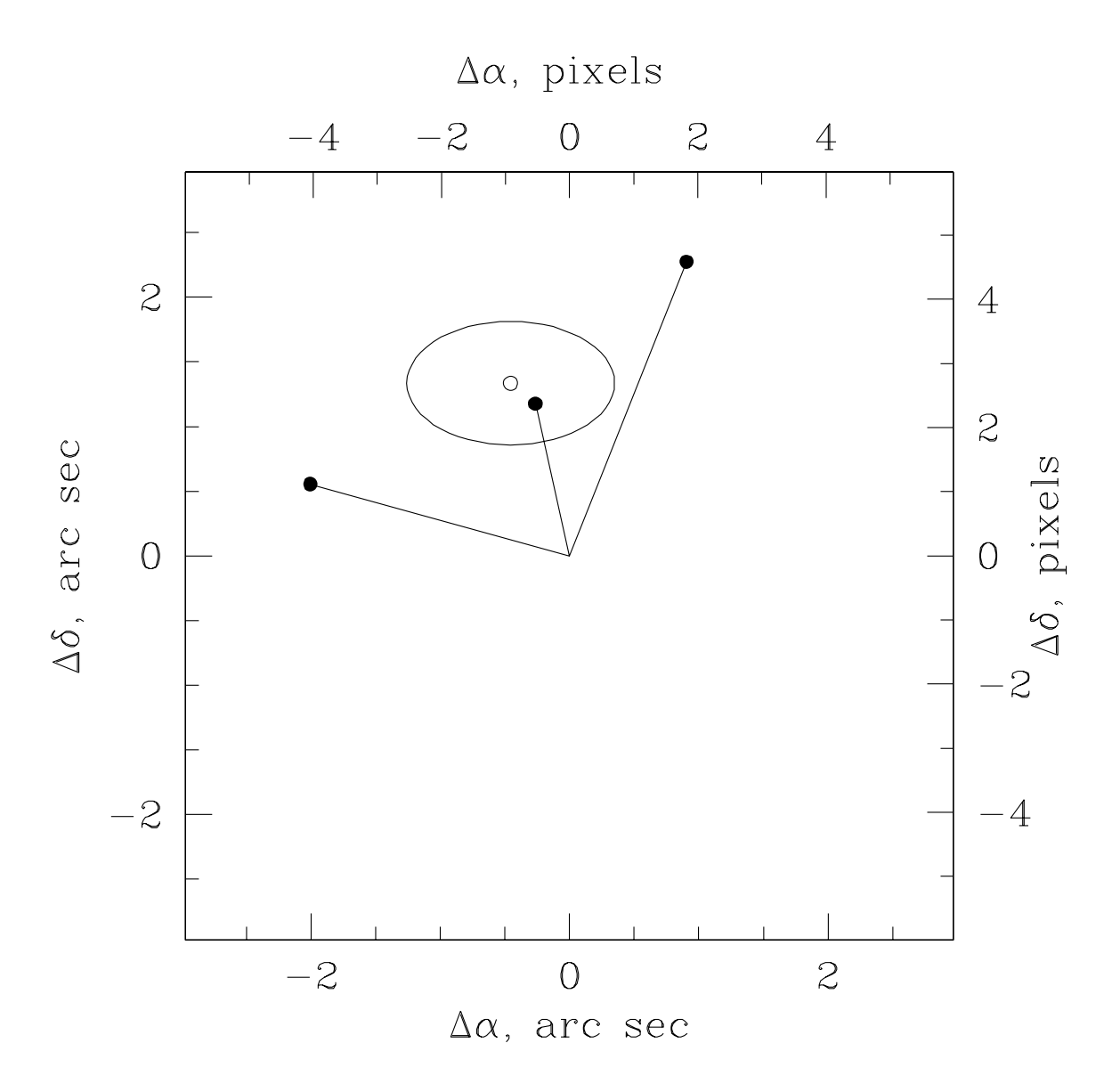


Fig. 4.— Positional offsets of the three USNO sources which appear as point sources on the Chandra fields.

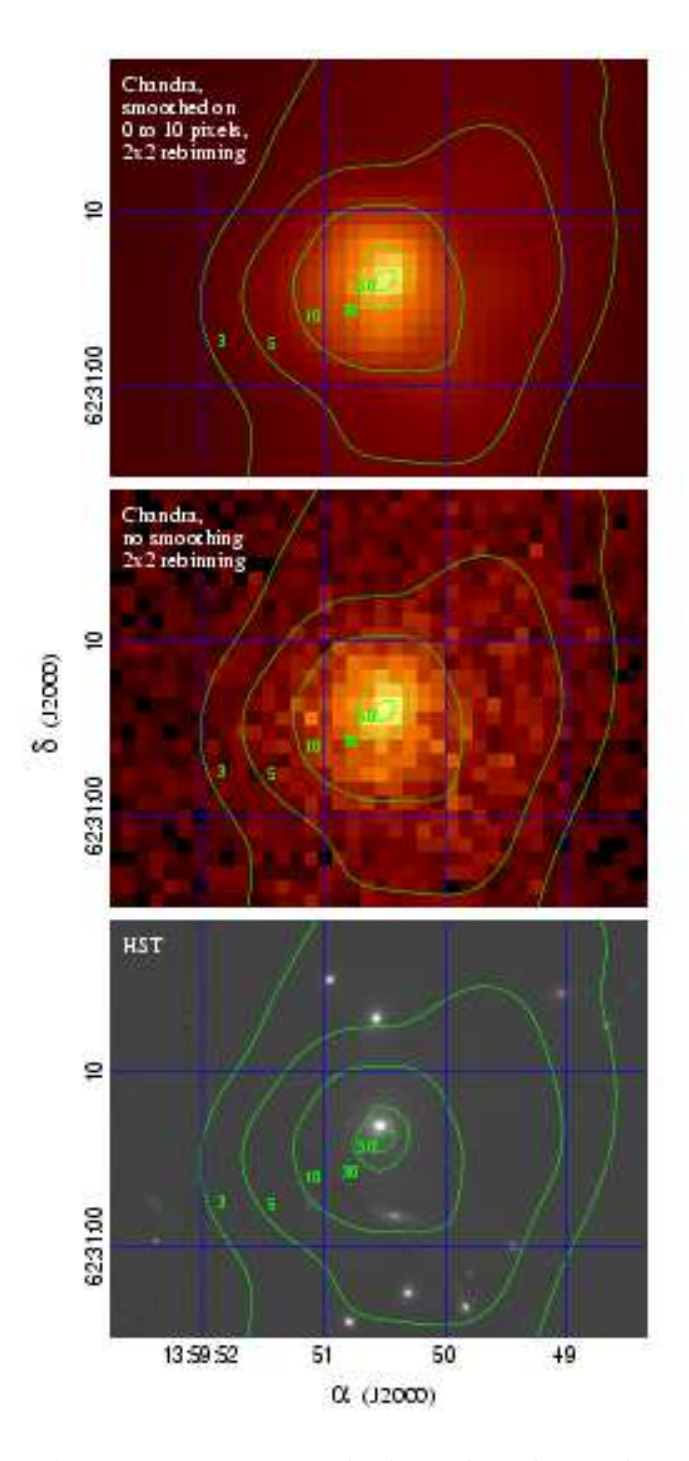


Fig. 5.— Broad-band X-ray contours overlaid on the adaptively smoothed Chandra X-ray image (top), the unsmoothed  $2 \times 2$ -binned image, and the HST field (bottom).

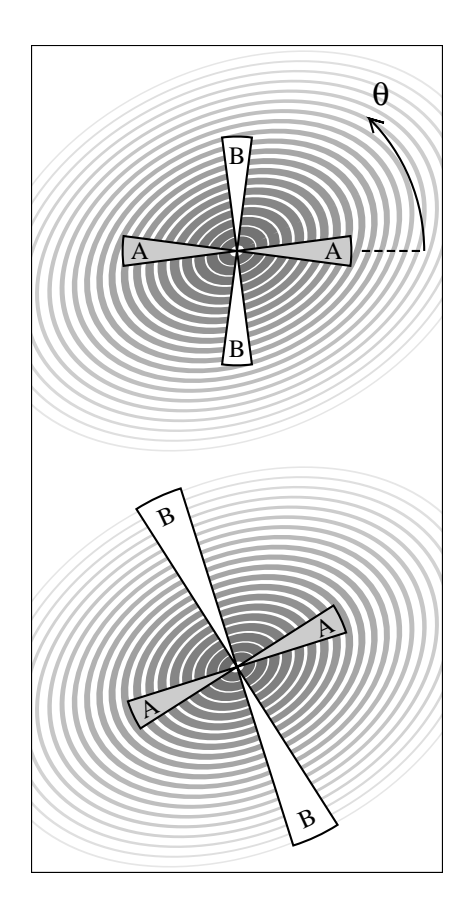


Fig. 6.— Wedge pairs used to estimate the cluster ellipticity. Wedges of equal radius are used first to determine the position angle, and then wedge B is scaled so that its luminosity is the same as wedge A.

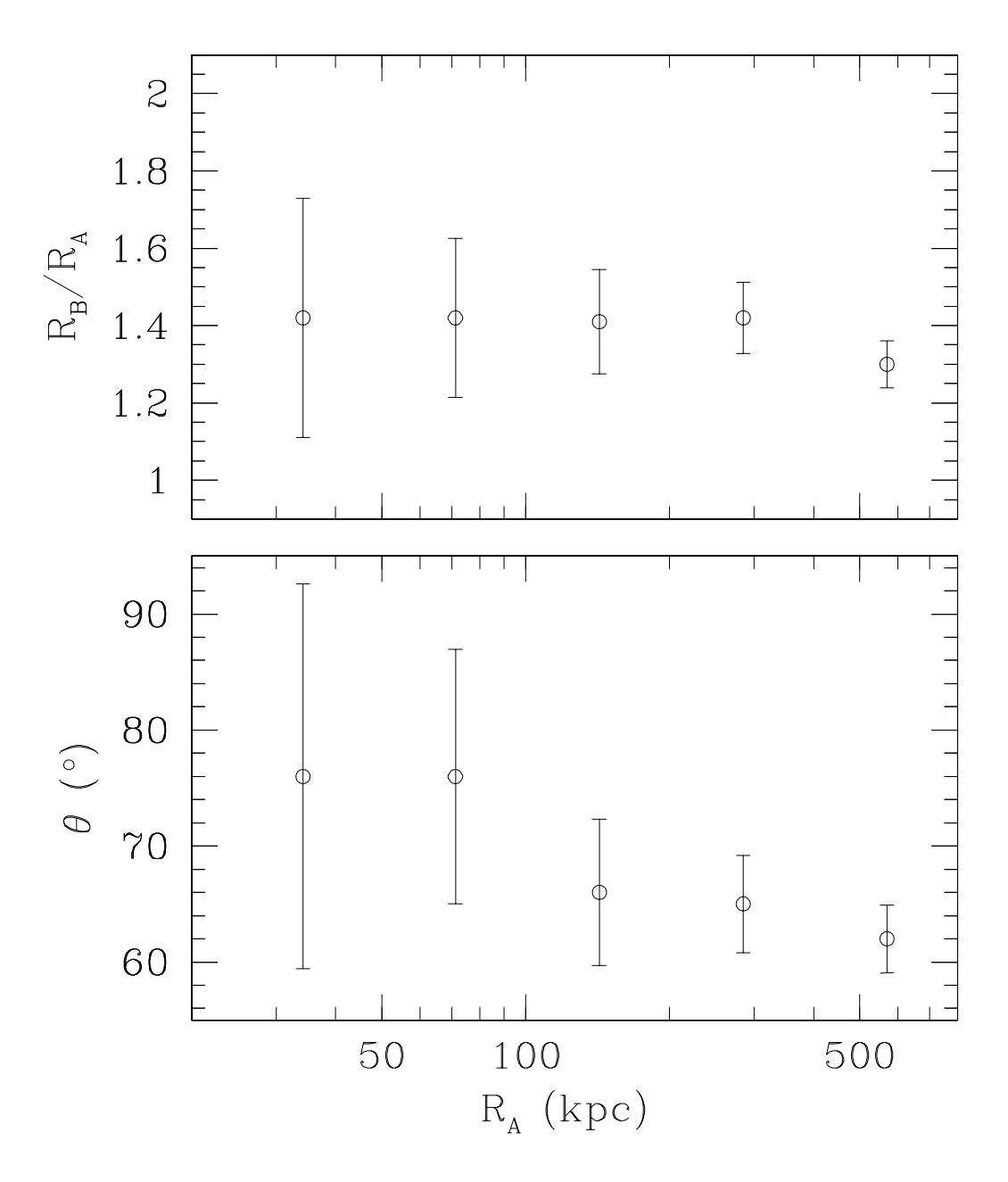


Fig. 7.— Radial dependence of the flattening and position angle. It should be noted that these quantities are calculated by integrating to  $R_A$ , and in that sense represent a radially cumulative average.

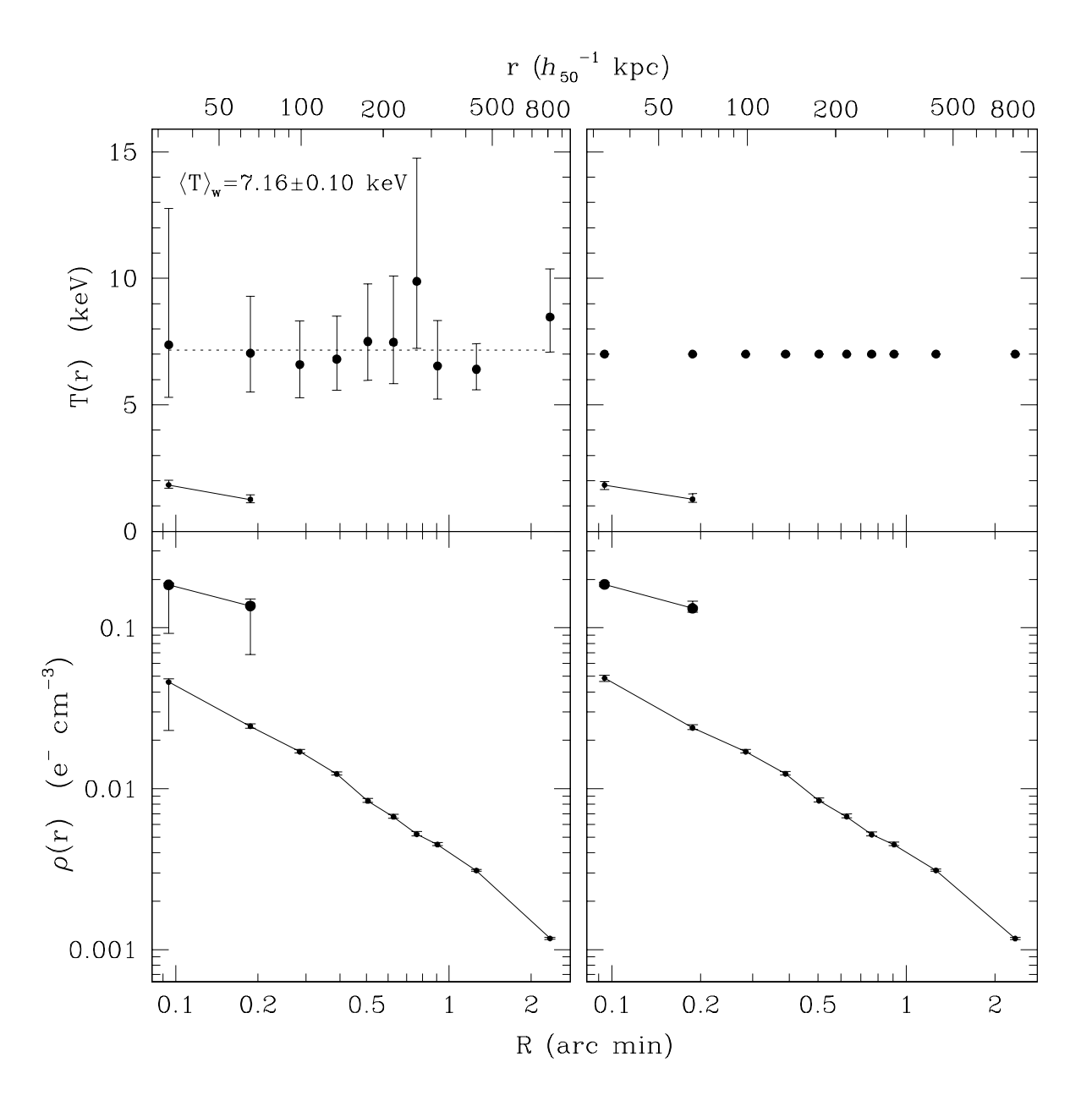


Fig. 8.— Deprojected radial temperature and density profiles of EMSS 1358. Note that the inner two annuli are represented by two emission components at different temperatures. The profiles on the left are calculated allowing the hot gas temperature to vary; those on the right are frozen at 7 keV.

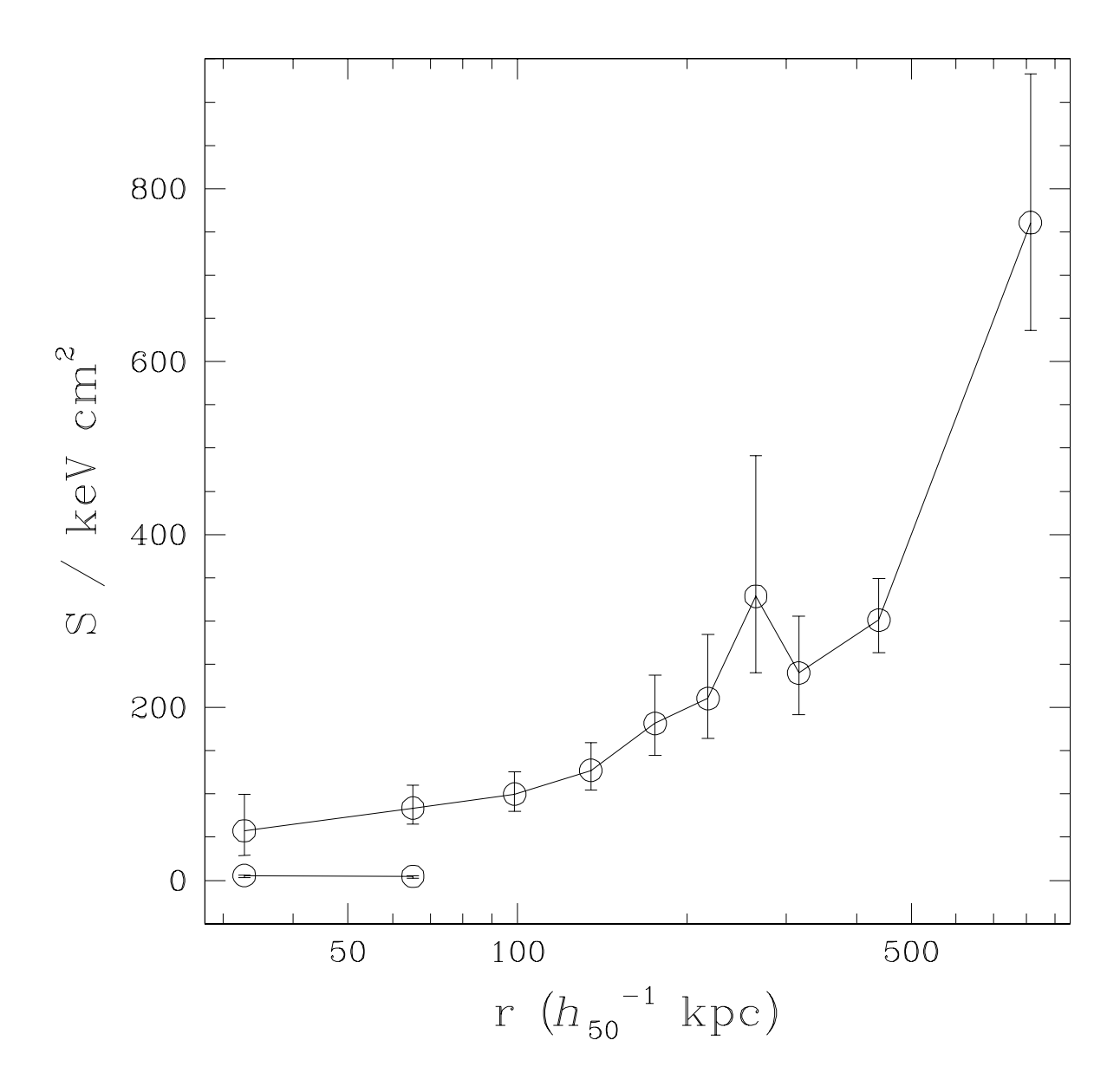


Fig. 9.— Entropy profile of EMSS 1358. The curve that spans the entire range in r represent the entropy of the gas at temperature  $T_h$ ; the short segment represents the gas at  $T_c$ .

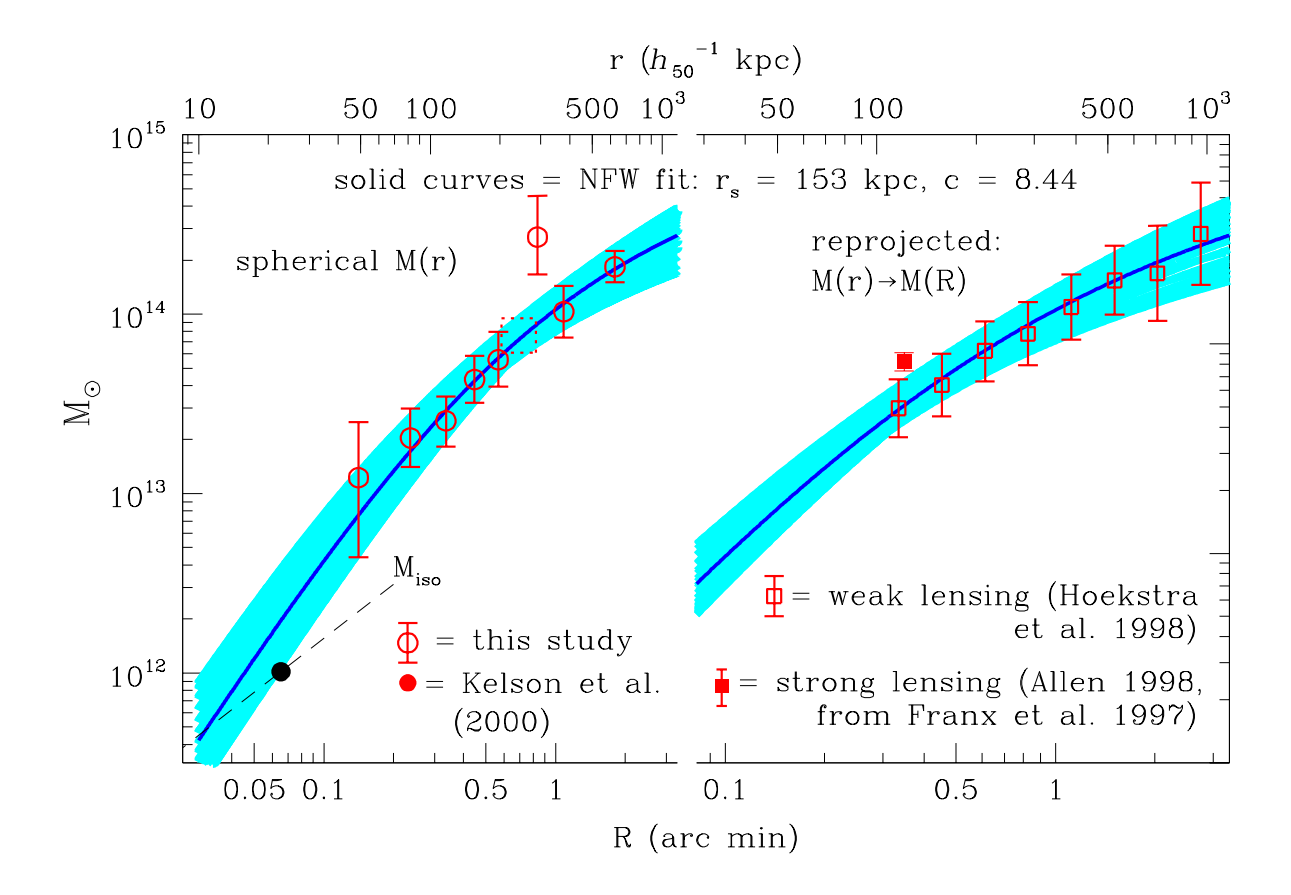


Fig. 10.— Deprojected mass profile of EMSS 1358. The data points in the left panel represent M(r), the mass contained within spherical radius r, calculated using the density and unrestricted temperature profile shown in the left panels of Figure 8, with the single unphysical point represented as a dashed box. The solid dark blue curve and light blue 1- $\sigma$  envelope represents the best-fit NFW profile. On the right the spherical NFW profile has been projected along the line of sight according to equation 15, in order to compare it to the weak lensing measurements of Hoekstra et al. (1998).

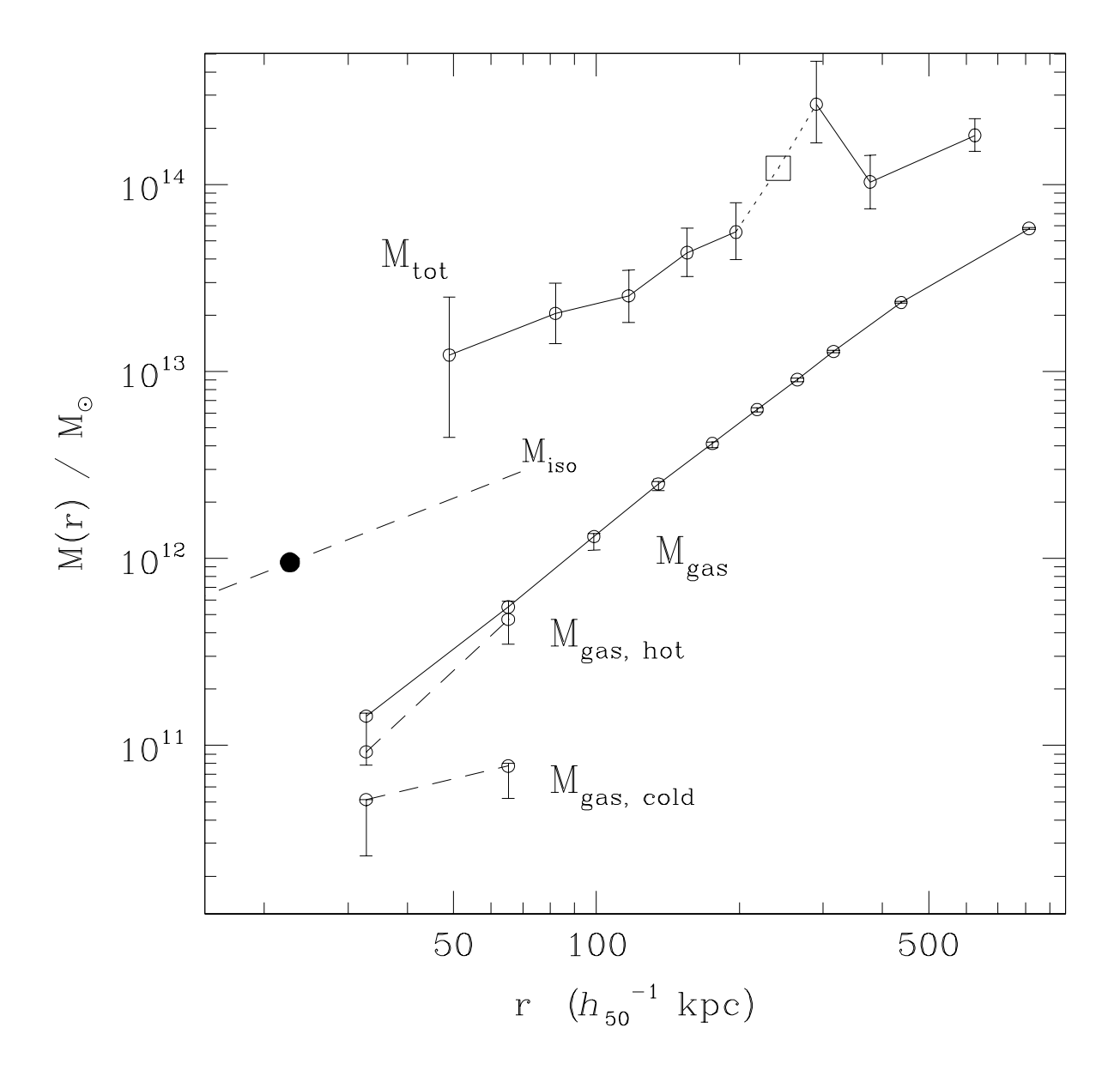


Fig. 11.— The total integrated gravitating mass and gas mass of EMSS 1358. The non-physical point (M(r) < 0) is represented by an open box in the total mass profile.

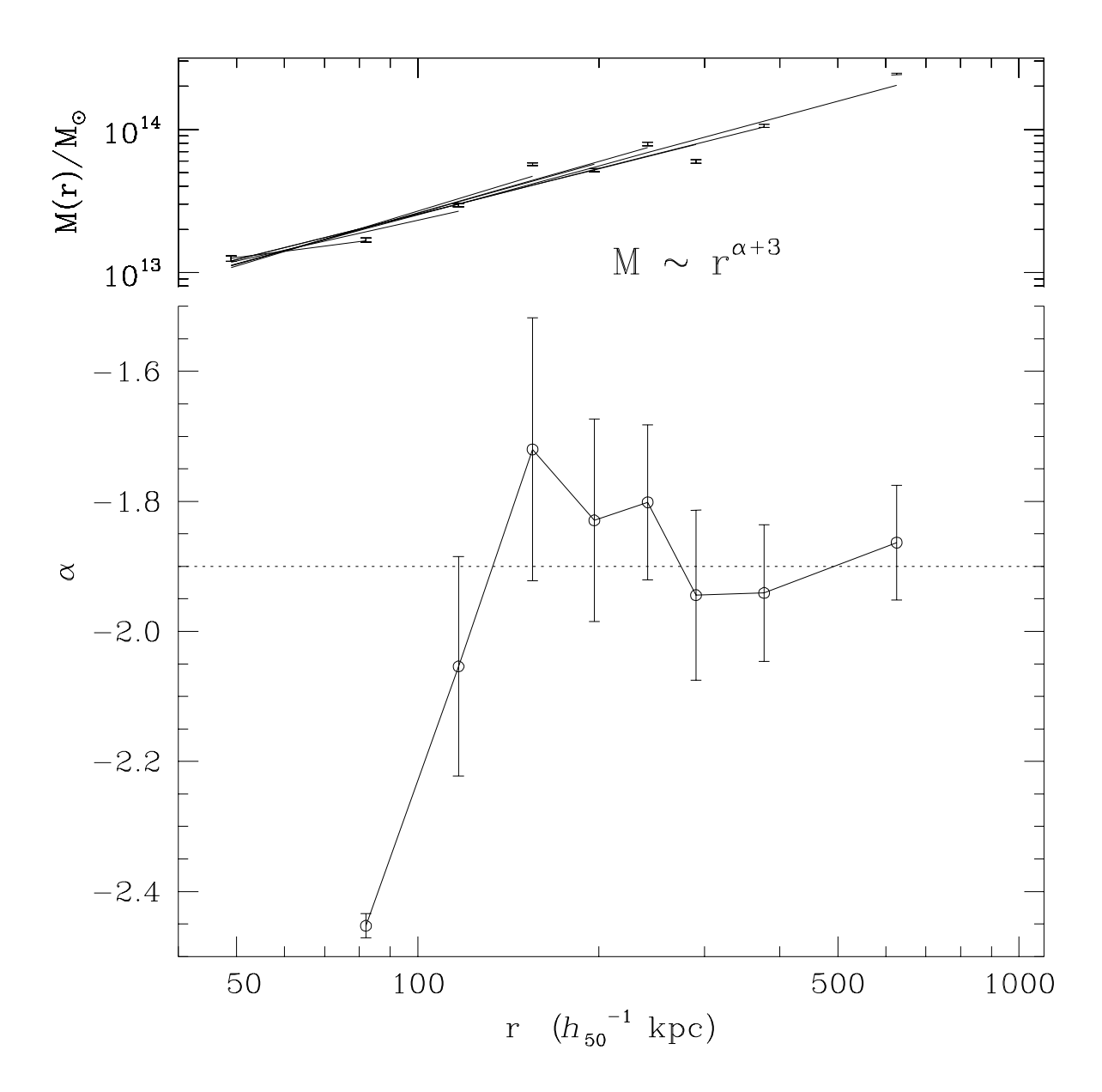


Fig. 12.— Power law fits to the mass profile of EMSS 1358. The top panel shows the mass profile for the  $T_h = 7$  keV model along with power law fits using points 1-k,  $k \in [2, 9]$ . The bottom panel shows the power law index of the fit, as a function of the radius of the outermost point used. Note that  $\alpha$  is the power law slope on  $\rho(r)$ , not M(r).

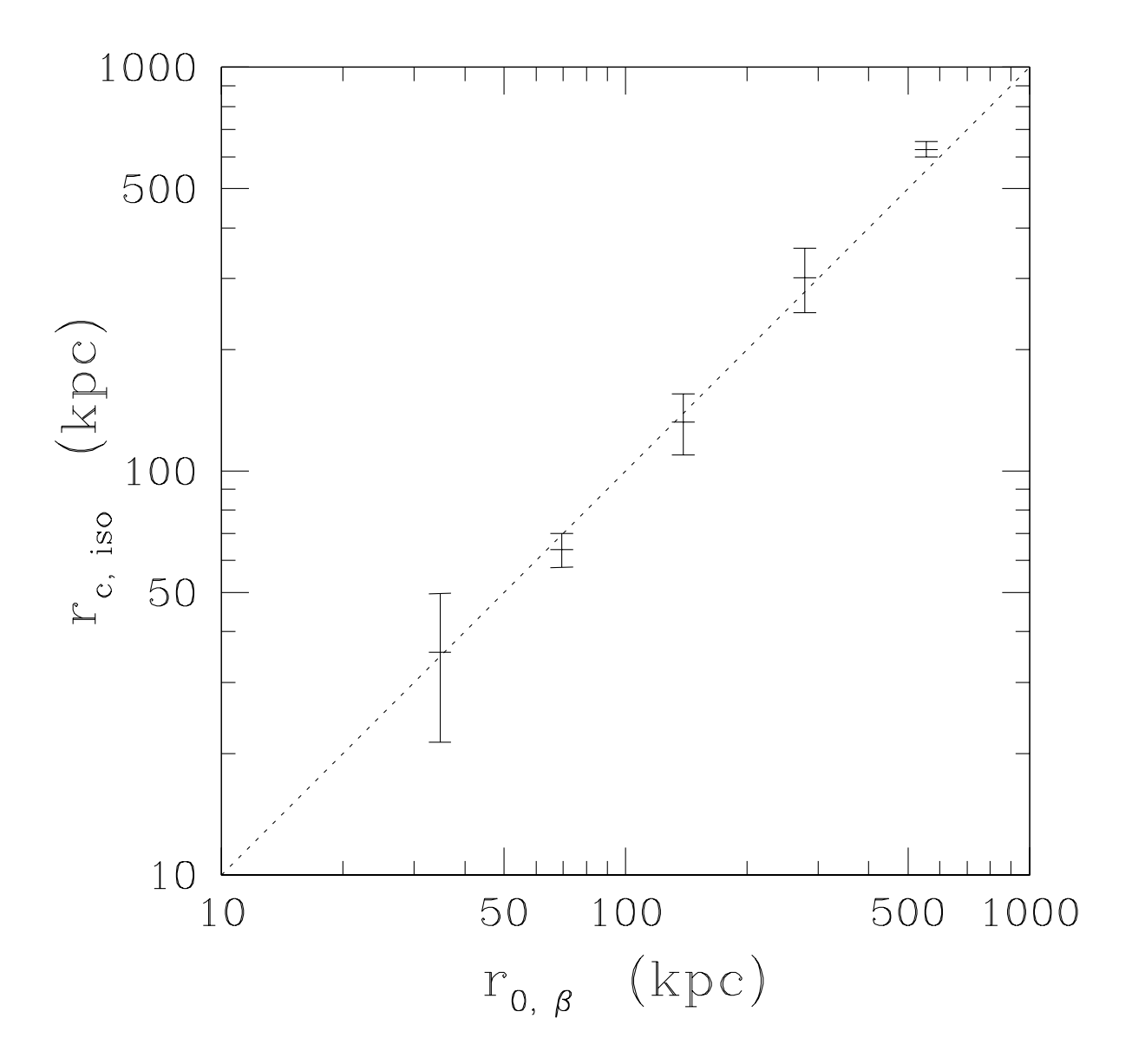


Fig. 13.— Softened isothermal sphere fits to a set of 5 simulated galaxy cluster observations which follow a  $\beta$  model profile. The fitted isothermal sphere core radius is plotted against the  $\beta$  model core radius.

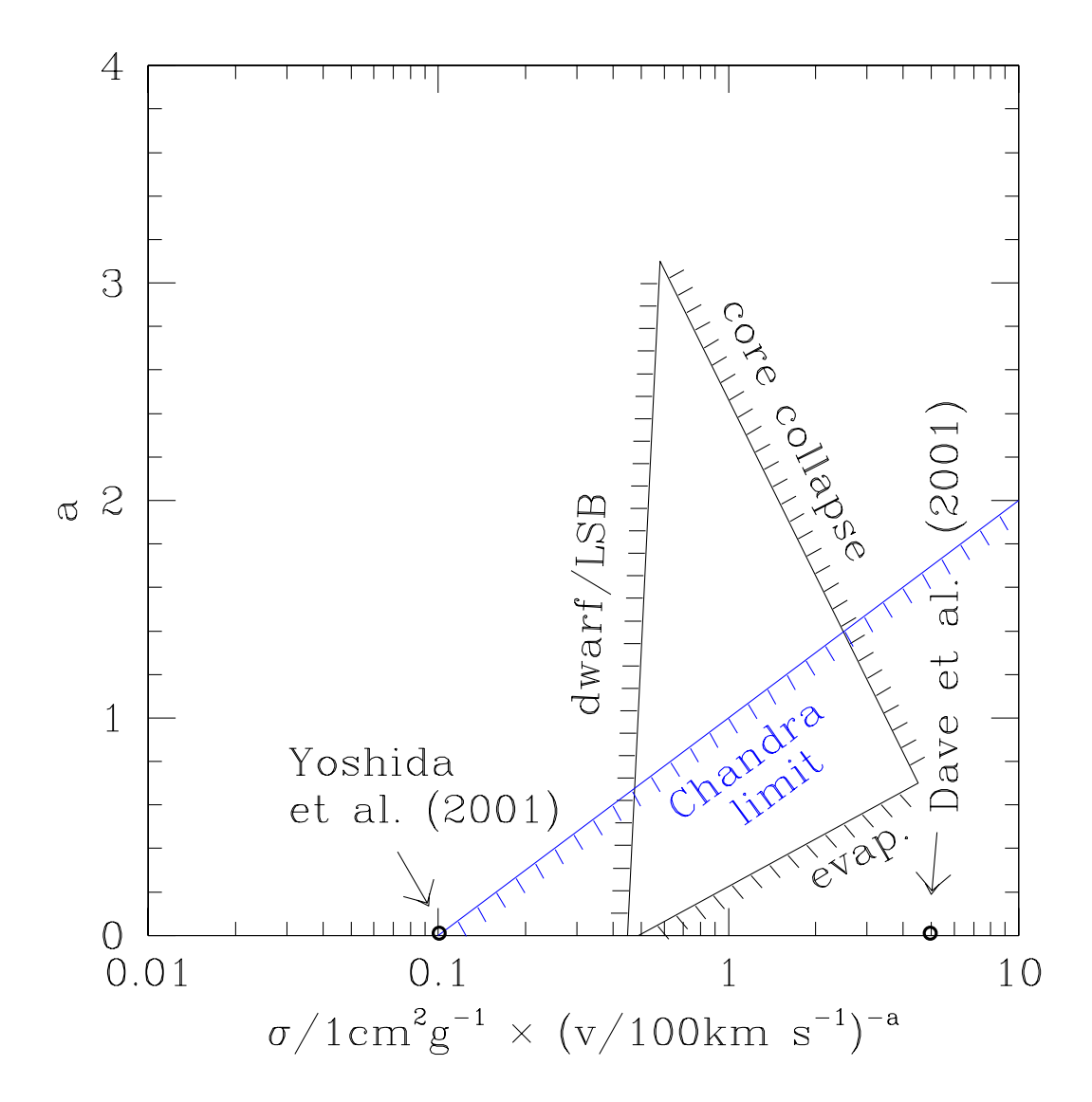


Fig. 14.— Constraints on the SIDM cross section, adapted from Hennawi & Ostriker (2001). The hatch marks delineate the region excluded by each constraint. The triangular region is derived from several astrophysical constraints of Hennawi & Ostriker (2001) (see text). The results of the simulations of Yoshida et al. (2000) and Davé et al. (2001) are indicated. The blue excluded region labeled 'Chandra limit' represents the constraint we derive from the absence of a significant core in the mass profile of EMSS 1358+6245.

 ${\bf Table\ 1.}\quad {\bf Source\ annuli\ statistics.}$ 

annulus	$R_{\rm pixel}$	$R_{\rm kpc}$	total photons	source photons
1	11.5	32.7	2019	2004
2	22.9	65.2	2004	1958
3	34.7	98.8	2005	1926
4	47.4	135.0	2007	1895
5	61.6	175.4	2000	1820
6	76.5	217.8	2000	1761
7	93.0	264.8	2007	1682
8	110.8	315.5	2011	1589
9	153.8	437.9	4013	2691
10	285.8	813.8	10040	3299

Table 2. Comparison of hot and cold gas in the inner two shells.

quantity	component	shell 1	shell 2
$T/\mathrm{keV}$	$\begin{array}{c} \operatorname{cold} \\ \operatorname{hot} \end{array}$	$1.83_{-0.13}^{+0.18} \\ 7.37_{-2.07}^{+5.40}$	$1.26_{-0.13}^{+0.18} \\ 7.04_{-1.54}^{+2.26}$
$\rho/10^{-26}~{\rm g~cm^{-3}}$	$   \begin{array}{c}     \text{cold} \\     \text{hot}   \end{array} $	$19.4_{-9.7}^{+0.5} \\ 4.83_{-2.42}^{+0.24}$	$14.4 \begin{array}{l} +1.5 \\ -7.2 \\ 2.57 ^{+0.08}_{-0.06} \end{array}$
$\delta M/10^{11}~M_{\odot}$	cold hot	$0.513_{-0.257}^{+0.013} \\ 0.923_{-0.462}^{+0.047}$	$\begin{array}{c} 0.264^{+0.027}_{-0.132} \\ 3.81 \begin{array}{c} ^{+0.105}_{-0.076} \end{array}$
$V/V_{ m total}$	cold hot	0.121 0.879	0.012 0.988